# Mechanical actions on nanocylinders in nematic liquid crystals

Geoff McKay
*Department of Mathematics, University of Strathclyde, 26 Richmond Street, Glasgow G1 1XH, United Kingdom*

Epifanio G. Virga
*Dipartimento di Matematica, Istituto Nazionale di Fisica della Materia, Università di Pavia, via Ferrata 1, 27100 Pavia, Italy*
(Received 16 December 2004; published 8 April 2005)

We apply the Landau–de Gennes theory to study the equilibrium problem that arises when a cylinder of radius $R$ is kept at a given distance $h$ from a plane wall. We assume that both the lateral boundary of the cylinder and the wall enforce *homeotropic* anchoring conditions on the liquid crystal, which prescribe the liquid crystal molecules to stick orthogonally to the bounding surfaces. Typically, in our study $R$ ranges from a few to hundreds of biaxial coherence lengths, where a biaxial coherence length, which depends on the temperature, is a few nanometers. The equilibrium textures exhibit a bifurcation between a *flat* solution, where one eigenvector of the order tensor $\mathbf{Q}$ is everywhere parallel to the cylinder's axis, and an *escape* solution, where the eigenframe of $\mathbf{Q}$ flips out of the plane orthogonal to the cylinder's axis. The escape texture minimizes an appropriately renormalized energy functional $\mathcal{F}^*$ for $h>h_c$, while the flat texture minimizes $\mathcal{F}^*$ for $h<h_c$. We compute both the force and the torque transmitted to the cylinder by the surrounding liquid crystal and we find that the diagrams of both as functions of $h$ fail to be monotonic along the escape texture. Thus, upon decreasing $h$, a snapping instability is predicted to occur, with an associated hysteresis loop in the force diagram, before $h$ reaches $h_c$. Finally, since the symmetry of this problem makes it equivalent to the one where two parallel cylinders are separated by the distance $2h$, the snapping instability predicted here should also be observed there.

DOI: 10.1103/PhysRevE.71.041702 PACS number(s): 61.30.Dk, 61.30.Gd, 61.30.Hn

## I. INTRODUCTION

Nematic liquid crystals are complex anisotropic fluids with variable molecular ordering. When rigid particles are submerged in these fluids, the molecular ordering is affected by the interactions of the molecules with the particles' boundaries. In turn, the change in ordering can result in an elastic distortion that induces a displacement or a rotation of the particle to relax the excess of energy associated with the distorting interactions [1]. This essentially explains the ability of nematic liquid crystals to exert forces and torques on submerged particles. Actually, when the submerged particles prescribe the nematic molecules to be aligned in the direction orthogonal to their boundaries (*homeotropic* anchoring), the intervening liquid crystal mediates an interaction between the particles that prompts the particles to acquire regular equilibrium patterns [2–6]. Despite the significance of these interactions, only a few direct measurements have so far become available [3,6,7].

Theoretically, when the particles' size becomes comparable to the length scale over which the molecular ordering is organized, typically between a few and ten nanometers, the conventional description of the molecular organization in terms of the nematic director $\boldsymbol{n}$ becomes insufficient. Both the forces and the torques exerted on a submerged particle must then be evaluated within the Landau–de Gennes theory, which employs a full second-rank tensor $\mathbf{Q}$ to describe the local molecular ordering. This paper is concerned with computing the force and the torque exerted on a nanocylinder surrounded by a liquid crystal confined in a half-space by a plane wall: under the assumption that both the cylinder and the wall prescribe homeotropic alignment on the liquid crystal molecules, we derive the force and the torque from a stress and a couple stress tensor appropriately defined within the Landau–de Gennes theory. This is by no means a mere academic study, since experiments with nanowires submerged in a liquid crystal have recently begun to be performed by Lapointe *et al.* [8], though with anchoring conditions that make it not mandatory to resort to the Landau–de Gennes theory to estimate the mechanical actions transmitted on the cylinder. In Lapointe *et al.*'s experiment, the ordering prescribed on the lateral boundary of the cylinder is parallel to the symmetry axis: the classical studies on mechanical actions in liquid crystals employing the director theory suffice there to describe the experimental results [9–11]. The case envisaged here requires an extended theory.

The paper is organized as follows. In Sec. II we describe the energy functional that governs the equilibrium configurations of liquid crystals in the theory adopted here and we present the associated stress and couple stress fields. In Sec. III, we introduce a special system of coordinates and a class of order tensor fields suitable for the equilibrium problem at hand. In Sec. IV, we solve numerically the equilibrium equations associated with an appropriately renormalized energy functional, and in Sec. V we explore the stability of these solutions. Section VI is devoted to the evaluation of both force and torque on the cylinder as functions of the separation between cylinder and wall: this analysis illustrates a lack of monotonicity in these diagrams with an associated hysteresis loop. The final section, Sec. VII, presents a discussion of our results. The paper is then closed by an Appendix, where we treat the case of a linearly elastic, flexible nanotubule submerged in a liquid crystal.

 

## II. ENERGY AND STRESSES

When the local order in liquid crystals varies in space, in response to either geometric confinements or applied external fields, the alignment of the elongated molecules that constitute the medium is described on a mesoscopic scale by the order tensor $\mathbf{Q}$. This is a symmetric, traceless tensor of rank two, whose eigenvalues range in the interval $[-1/3, 2/3]$. When two eigenvalues of $\mathbf{Q}$ are equal to one another, the corresponding state is said to be *uniaxial* and can be represented in the form

$$\mathbf{Q} = s\left(\boldsymbol{n} \otimes \boldsymbol{n} - \tfrac{1}{3}\mathbf{I}\right), \tag{1}$$

where $\mathbf{I}$ is the identity tensor, $\boldsymbol{n}$ is the nematic *director*, and $s \in [-1/2, 1]$ is the *scalar* order parameter. Positive values of $s$ represent uniaxial states where the molecules exhibit a more or less pronounced tendency to align in the direction of $\boldsymbol{n}$, whereas negative values of $s$ represent states where the molecules exhibit a tendency to lie in the plane orthogonal to $\boldsymbol{n}$. In general, when all three eigenvalues of $\mathbf{Q}$ are different from one another, there is not a single director and $\mathbf{Q}$ is represented in the form

$$\mathbf{Q} = s_1 \boldsymbol{e}_1 \otimes \boldsymbol{e}_1 + s_2 \boldsymbol{e}_2 \otimes \boldsymbol{e}_2 - (s_1 + s_2)\boldsymbol{e}_3 \otimes \boldsymbol{e}_3, \tag{2}$$

where $(\boldsymbol{e}_1, \boldsymbol{e}_2, \boldsymbol{e}_3)$ is the eigenframe of $\mathbf{Q}$, and $s_1$, $s_2$ and $s_3 = -(s_1 + s_2)$ are the corresponding eigenvalues. A state represented by $\mathbf{Q}$ as in Eq. (2) is said to be *biaxial*. An invariant measure of biaxiality is given by [12]

$$\beta^2 := 1 - 6\frac{(\operatorname{tr}\mathbf{Q}^3)^2}{(\operatorname{tr}\mathbf{Q}^2)^3}. \tag{3}$$

This parameter ranges in $[0, 1]$ and vanishes precisely for all uniaxial states of $\mathbf{Q}$.

In the absence of any external disturbing influence, below the nematic-isotropic transition temperature $T_{NI}$, the state naturally preferred by a nematic liquid crystal comprising essentially cylindrical molecules would be uniaxial. This property is reflected by the minimizer of the bulk potential $f_b$. In this paper we adopt for $f_b$ the following classical expression:

$$f_b(\mathbf{Q}) = \frac{A}{2}\operatorname{tr}\mathbf{Q}^2 - \frac{B}{3}\operatorname{tr}\mathbf{Q}^3 + \frac{C}{4}(\operatorname{tr}\mathbf{Q}^2)^2. \tag{4}$$

Here both $B$ and $C$ are positive scalars, and $A$, which is the only parameter assumed to depend on the temperature $T$, is given the form

$$A = a(T - T^*), \tag{5}$$

where $a$ is a positive constant and $T^* < T_{NI}$ is the *supercooling* temperature. The value $A_{NI}$ of $A$ at the nematic-isotropic transition, which defines $T_{NI}$ through Eq. (5), is given by

$$A_{NI} = \frac{B^2}{27C}.$$

It is easily shown [13] that the relative and absolute minimizers of $f_b$ satisfy $\beta^2 = 0$. Moreover, the order tensors that minimize $f_b$ for $T < T_{NI}$ can be represented as in Eq. (1) with arbitrary $\boldsymbol{n}$ and

$$s = s_b := \frac{B + \sqrt{B^2 - 24AC}}{4A}. \tag{6}$$

We find it convenient to define the reduced temperature $\theta$ as [13]

$$\theta := \frac{24AC}{B^2} = \frac{T - T^*}{T^{**} - T^*}, \tag{7}$$

where $T^{**} > T_{NI}$ is the *superheating* temperature. A useful consequence of this definition is that we can write $A$ in the form

$$A = \theta A_*,$$

where $A_* := B^2/24C$ is the value of $A$ at the superheating temperature. Other authors [14–16] prefer to define another reduced temperature, that is,

$$\tau := \frac{T - T^*}{T_{NI} - T^*}.$$

It is easily seen that $\theta = \frac{8}{9}\tau$. Similarly, we introduce the equilibrium value of the scalar order parameter $s$ at the superheating temperature

$$s_* := \frac{B}{4C}, \tag{8}$$

so that the equilibrium value of $s$ at the temperature $T < T^{**}$ can be expressed as

$$s_b = s_* \hat{s}_b \quad \text{with} \quad \hat{s}_b := 1 + \sqrt{1 - \theta}. \tag{9}$$

When the tensor field $\mathbf{Q}$ is not uniform in space, we write the free energy $W$ per unit volume in the form

$$W = \frac{L}{2}|\nabla\mathbf{Q}|^2 + f_b(\mathbf{Q}), \tag{10}$$

where $L$ is a positive elastic constant independent of temperature. Thus, if $\mathcal{B}$ is any region in space occupied by the liquid crystal, the total free energy $\mathbb{F}(\mathcal{B})$ stored in $\mathcal{B}$ can be represented as

$$\mathbb{F}(\mathcal{B}) = \int_{\mathcal{B}} W \, \mathrm{d}V,$$

where $V$ is the volume measure. In the absence of body torques exerted by external causes, such as electric or magnetic fields, an equilibrium configuration for $\mathbb{F}(\mathcal{B})$ satisfies the equation [17]

$$\operatorname{div}\mathbf{T}^{(E)} = \mathbf{0}, \tag{11}$$

where

$$\mathbf{T}^{(E)} := W\mathbf{I} - \nabla\mathbf{Q} \odot \frac{\partial W}{\partial \nabla\mathbf{Q}} \tag{12}$$

and the tensor product $\odot$ is defined so that, in Cartesian components,

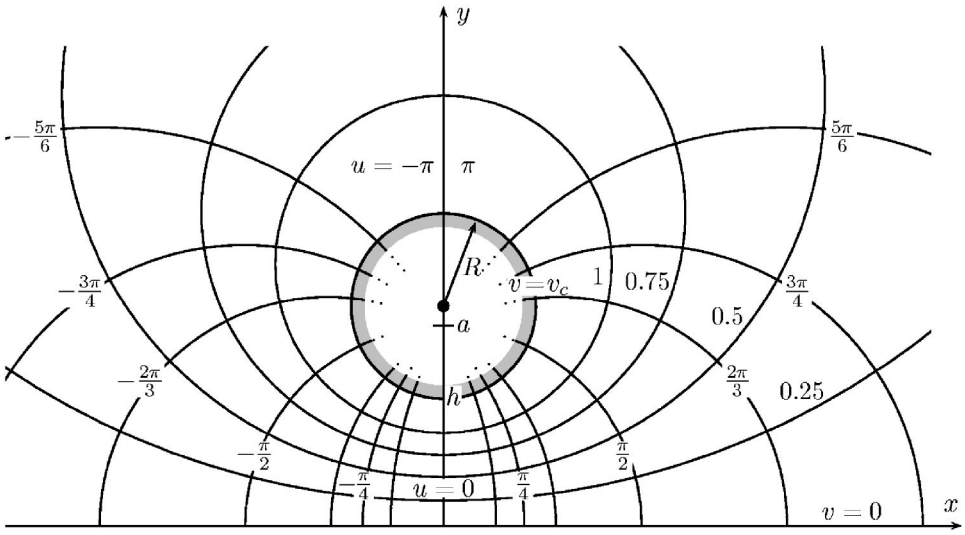


FIG. 1. The orthogonal circles in the $(x,y)$ plane representing the $(u,v)$ coordinate lines. The circles in Eq. (19a) corresponding to all values of $u_0$ in $]-\pi,\pi]$ meet at the points $\{x=0,y=\pm a\}$. The cross section of cylinder $\mathcal{C}$ with radius $R$ coincides with the coordinate circle $v=v_c$.

$$\left(\nabla\mathbf{Q}\odot\frac{\partial W}{\partial\nabla\mathbf{Q}}\right)_{ij}=Q_{hk,i}\frac{\partial W}{\partial Q_{hk,j}}.$$

Here and in the following we adopt the convention of summing over repeated indices. $\mathbf{T}^{(E)}$ is the form of Ericksen's stress tensor appropriate for the present tensorial formulation of the equilibrium theory. It extends the classical definition originally given within the director theory [9,18]. Formally, Eq. (11) is obtained from a domain variation of $\mathbb{F}(\mathcal{B})$, in the same spirit as in Ref. [19]. The stress tensor represents the distribution of contact forces in $\mathcal{B}$. In particular, for any body $\mathcal{P}$ submerged in $\mathcal{B}$ the total force $\boldsymbol{F}(\mathcal{P})$ transmitted by the liquid crystal through the boundary $\partial\mathcal{P}$ is given by

$$\boldsymbol{F}(\mathcal{P})=\int_{\partial\mathcal{P}}\mathbf{T}^{(E)}\boldsymbol{\nu}\,\mathrm{d}S, \tag{13}$$

where $\boldsymbol{\nu}$ is the outer unit normal to $\partial\mathcal{P}$ and $S$ is the area measure.

Similarly, the distribution of contact torques is described by the couple stress tensor $\mathbf{L}$, whose Cartesian components $L_{ij}$ are expressed as [20–22]

$$L_{ij}=2\varepsilon_{ikl}Q_{km}\frac{\partial W}{\partial Q_{ml,j}}, \tag{14}$$

where $\varepsilon_{ikl}$ is Ricci's alternator. The tensor defined by Eq. (14) extends the couple stress tensor introduced by Leslie [23] within the director theory, and so we call it Leslie's couple stress tensor. It can be shown that both $\mathbf{T}^{(E)}$ and $\mathbf{L}$ reduce to their classical counterparts in the director theory whenever $\mathbf{Q}$ is given the form in Eq. (1) with a scalar order parameter $s$ uniform in space. In complete analogy with Eq. (13), the total torque $\boldsymbol{M}(\mathcal{P})$ transmitted on a submerged body $\mathcal{P}$ by the surrounding liquid crystal is provided by

$$\boldsymbol{M}(\mathcal{P})=\int_{\partial\mathcal{P}}\mathbf{L}\boldsymbol{\nu}\,\mathrm{d}S. \tag{15}$$

## III. MODEL

In this section we describe the geometric setting for the problem studied in this paper and we collect all the mathematical preliminaries needed to compute the mechanical actions on a solid cylinder submerged in a liquid crystal.

### A. Geometry

We consider the region $\mathcal{B}$ between an infinite circular cylinder $\mathcal{C}$ with radius $R$ and a plane parallel to the axis of $\mathcal{C}$, separated from the cylinder's lateral surface by a distance $h$. We assume that in a system of Cartesian coordinates $(x,y,z)$ the cylinder axis is chosen along $z$, so that the region $\mathcal{B}$ is described by the inequalities (see Fig. 1)

$$y>0 \quad \text{and} \quad x^2+(y-R-h)^2>0. \tag{16}$$

In the plane $(x,y)$, we introduce the system of *bipolar* coordinates $(u,v)$ defined so that

$$x=a\frac{\sin u}{\cos u+\cosh v}, \tag{17a}$$

$$y=a\frac{\sinh v}{\cos u+\cosh v}, \tag{17b}$$

where

$$\frac{a}{R}:=\sqrt{\left(\frac{h}{R}\right)^2+2\frac{h}{R}}. \tag{18}$$

The coordinates lines in the $(u,v)$ plane are families of orthogonal circles in the $(x,y)$ plane: for given values $u_0$ of $u$ and $v_0$ of $v$, these families are represented by the equations

$$(x+a\cot u_0)^2+y^2=\frac{a^2}{\sin^2 u_0}, \tag{19a}$$

$$x^2+(y-a\coth v_0)^2=\frac{a^2}{\sinh^2 v_0}. \tag{19b}$$

These are known as Apollonian circles: each of them is the locus of the points whose distances from two given points of

the $(x,y)$ plane are in a prescribed ratio, different for different circles [24]. It is easily seen that the circles in Eq. (19a) corresponding to all values of $u_0$ in $]-\pi,\pi]$ meet at the points $\{x=0, y=\pm a\}$. The parameter $a$ as defined in Eq. (18) is precisely the one that makes the cross section of $\mathcal{C}$ coincide with the coordinate circle at $v=v_c$. Moreover, in the coordinates $(u,v)$ the region $\mathcal{B}$ is described by the inequalities

$$-\pi < u \leqslant \pi \quad \text{and} \quad 0 < v < v_c \quad \text{where} \quad v_c := \sinh^{-1}\frac{a}{R}, \tag{20}$$

which follow easily from inequalities (16) and Eqs. (19). As shown in Fig. 1, the half-line $\{x=0, y>h+2R\}$ is attained in both limits as $u\to-\pi$ and $u\to\pi$, while the segment $\{x=0, 0<y<h\}$ corresponds to $u=0$. Moreover, $u$ is positive in the half-space $\{x>0\}$ and negative in the half-space $\{x<0\}$. The Jacobian determinant of the change of variables $(x,y)\to(u,v)$ is

$$J = \frac{a^2}{(\cos u + \cosh v)^2}. \tag{21}$$

With the aid of Eqs. (19), we derive the following formulas for the unit vectors $\boldsymbol{e}_u$ and $\boldsymbol{e}_v$ tangent to the $(u,v)$ coordinate lines:

$$\boldsymbol{e}_u = \frac{1+\cos u\cosh v}{\cos u+\cosh v}\boldsymbol{e}_x + \frac{\sin u\sinh v}{\cos u+\cosh v}\boldsymbol{e}_y, \tag{22a}$$

$$\boldsymbol{e}_v = -\frac{\sin u\sinh v}{\cos u+\cosh v}\boldsymbol{e}_x + \frac{1+\cos u\cosh v}{\cos u+\cosh v}\boldsymbol{e}_y. \tag{22b}$$

For later use, we also record here the expressions for the spacial gradients of these fields:

$$\nabla\boldsymbol{e}_u = \frac{1}{a}[(\sinh v)\boldsymbol{e}_v\otimes\boldsymbol{e}_u + (\sin u)\boldsymbol{e}_v\otimes\boldsymbol{e}_v], \tag{23a}$$

$$\nabla\boldsymbol{e}_v = -\frac{1}{a}[(\sinh v)\boldsymbol{e}_u\otimes\boldsymbol{e}_u + (\sin u)\boldsymbol{e}_u\otimes\boldsymbol{e}_v]. \tag{23b}$$

### B. Mechanical actions

We adopt the following representation for the order tensor $\mathbf{Q}$:

$$\mathbf{Q} = s_1\boldsymbol{e}_u\otimes\boldsymbol{e}_u + s_2\boldsymbol{e}_2\otimes\boldsymbol{e}_2 - (s_1+s_2)\boldsymbol{e}_3\otimes\boldsymbol{e}_3, \tag{24}$$

where

$$\boldsymbol{e}_2 = (\cos\phi)\boldsymbol{e}_v + (\sin\phi)\boldsymbol{e}_z, \tag{25a}$$

$$\boldsymbol{e}_3 = -(\sin\phi)\boldsymbol{e}_v + (\cos\phi)\boldsymbol{e}_z, \tag{25b}$$

and $s_1$, $s_2$, and $\phi$ are all functions of $v$ alone. According to Eq. (24), $\boldsymbol{e}_u$ is an eigenvector of $\mathbf{Q}$ everywhere in $\mathcal{B}$, while the eigenvector $\boldsymbol{e}_2$ can somewhere flip out of the $(x,y)$ plane, orthogonal to the cylinder axis. The eigenframe of $\mathbf{Q}$ coincides with the coordinate frame $\{\boldsymbol{e}_u,\boldsymbol{e}_v,\boldsymbol{e}_z\}$ only where $\phi=0$.

On both the plane and the cylinder that bound $\mathcal{B}$, the order tensor $\mathbf{Q}$ is prescribed to be uniaxial with nematic director along the normal to the bounding surface and scalar order parameter $s=s_b$. These boundary conditions are also called *homeotropic*: in terms of the variables $s_1$, $s_2$, and $\phi$, they read as

$$s_1|_{\partial\mathcal{B}} = -\tfrac{1}{3}s_b, \quad s_2|_{\partial\mathcal{B}} = \tfrac{2}{3}s_b, \quad \phi|_{\partial\mathcal{B}} = 0. \tag{26}$$

The purpose of our mathematical model is to compute accurately both the force and the torque exerted by the plane at $z=0$ on the cylinder $\mathcal{C}$ through the intervening liquid crystal. In particular, we will illuminate the role played in this interaction by the biaxial states that are likely to arise in the liquid crystal in response to the geometric frustration it suffers, especially in the vicinity of the cylinder's surface, as a result of the boundary conditions imposed there.

We shall see in the following sections how the mechanical actions transmitted from the bounding plane to the submerged cylinder depend on both the cylinder radius $R$ and the distance $h$ between the cylinder and the plane; here, we remark instead that the symmetry of the boundary conditions allows us to establish that the same force and torque would be exchanged between *two* parallel cylinders of equal radius $R$ at the distance $2h$. Thus, our calculations will also be applicable to a surface force apparatus [25,26] with parallel cylinders. This allows our predictions to be subject to experimental validation.

Whenever $\mathbf{Q}$ is represented as in Eq. (24), $f_b$ in Eq. (4) becomes

$$f_b(\mathbf{Q}) = \hat{f}_b(s_1,s_2) = A(s_1^2+s_2^2+s_1s_2) + Bs_1s_2(s_1+s_2) + C(s_1^2+s_2^2+s_1s_2)^2. \tag{27}$$

Moreover,

$$|\nabla\mathbf{Q}|^2 = \frac{2}{a^2}[s_1'^2+s_1's_2'+s_2'^2+(s_1+2s_2)^2\phi'^2]\times(\cosh v+\cos u)^2 + \frac{2}{a^2}\left[(s_2-s_1)^2+\frac{3}{2}s_1\times(s_1+2s_2)(1-\cos 2\phi)\right](\cosh^2 v-\cos^2 u). \tag{28}$$

Since the outer unit normal $\boldsymbol{\nu}$ to $\mathcal{C}$ is $\boldsymbol{\nu}=-\boldsymbol{e}_v$, also by use of Eq. (12), we arrive at the following expression for the traction exerted on the cylinder's lateral boundary $\partial\mathcal{C}$ by the surrounding liquid crystal:

$$\mathbf{T}^{(E)}\boldsymbol{\nu}|_{\partial\mathcal{C}} = \frac{L}{a^2}\{2\sinh v\sin u[(q_1-q_2)^2+q_3^2]\boldsymbol{e}_u + [(\cosh v+\cos u)^2(q_1'^2+q_1'q_2'+q_2'^2+q_3'^2) + ((q_1-q_2)^2+q_3^2)(2\sin^2 u+\cos^2 u-\cosh^2 v) - f_b]\boldsymbol{e}_v\}_{v=v_c}, \tag{29}$$

where we have introduced the auxiliary variables

$$q_1 := s_1, \quad q_2 := \tfrac{1}{2}[-s_1 + (2s_2 + s_1)\cos 2\phi], \qquad q_3 := \tfrac{1}{2}(2s_2 + s_1)\sin 2\phi. \tag{30}$$

Similarly, the torque density is given by

$$\mathbf{L}\boldsymbol{\nu}|_{\partial\mathcal{C}} = \frac{2L}{a}((\cos u + \cosh v)[q_3'(q_1 + 2q_2) - q_3(q_1' + 2q_2')]\boldsymbol{e}_u + 3\sin u\{q_1 q_3 \boldsymbol{e}_v + [(q_1 - q_2)^2 + q_3^2]\boldsymbol{e}_z\})_{v=v_c}. \tag{31}$$

By Eqs. (13) and (15), the total force $\boldsymbol{f}$ and the total torque $\boldsymbol{m}$ exerted on $\partial\mathcal{C}$ per unit height of the cylinder are correspondingly given by the following integrals:

$$\boldsymbol{f} = \int_{-\pi}^{\pi} \mathbf{T}^{(E)}\boldsymbol{\nu}|_{\partial\mathcal{C}} \frac{a}{\cos u + \cosh v_c} \mathrm{d}u, \tag{32}$$

$$\boldsymbol{m} = \int_{-\pi}^{\pi} \mathbf{L}\boldsymbol{\nu}|_{\partial\mathcal{C}} \frac{a}{\cos u + \cosh v_c} \mathrm{d}u. \tag{33}$$

## IV. EQUILIBRIUM

Here we derive the equilibrium equations associated with the energy functional $\mathbb{F}(\mathcal{B})$. Before doing so, however, since the region $\mathcal{B}$ described above is unbounded, we need to extract from $\mathbb{F}(\mathcal{B})$ a meaningful convergent energy.

### A. Renormalized energy

We denote by $\mathcal{F}$ the total free energy stored in $\mathcal{B}$ per unit height of the cylinder $\mathcal{C}$. This energy, if computed as the integral of $W$ over the cross section of $\mathcal{B}$ with the $(x,y)$ plane, is bound to diverge. There are indeed in $W$ two distinct sources of divergence. First, the *condensation* energy for the nematic phase, that is, the minimum of $f_b$ in the nematic state does not vanish in the energy normalization chosen so far, and so the integral of $f_b$ over $\mathcal{B}$ clearly diverges as $\mathcal{B}$ is unbounded. Second, the far nematic field induced by the homeotropic boundary conditions is known to bear a divergent total elastic energy, similar to the energy surrounding a +1 disclination. A *renormalized* energy functional $\mathcal{F}^*$ is to be defined, which can be identified with $\mathcal{F}$ deprived of all its divergent parts: $\mathcal{F}^*$ would then represent the finite energy associated with the changes introduced in the far tensor field near the bounding surfaces of $\mathcal{B}$. The first source of divergence is easily suppressed by subtracting from $f_b$ in $W$ its minimum

$$\hat{f}_b\left(-\tfrac{1}{3}s_b, \tfrac{2}{3}s_b\right) = \tfrac{1}{36}Bs_b^3\left(\tfrac{1}{3} - \sqrt{1-\theta}\right).$$

To suppress the second source of divergence, we need to subtract from the elastic energy density its nonintegrable part, whose expression depends on the choice of coordinates. In the coordinates $(u,v)$ and under the assumption that $s_1$, $s_2$, and $\phi$ depend only on $v$, $\mathcal{F}^*$ can be given the following expression:

$$\mathcal{F}^* = \int_{-\pi}^{\pi} \mathrm{d}u \int_0^{v_c} \mathrm{d}v \left\{ \frac{L}{a^2} s_*^2 \left[ (s'^2_1 + s'^2_2 + s'_1 s'_2 + (s_1 + 2s_2)^2 \phi'^2) \times (\cosh v + \cos u)^2 + \left( (s_2 - s_1)^2 + \frac{3}{2} s_1 (s_1 + 2s_2)(1 - \cos 2\phi) \right) (\cosh^2 v - \cos^2 u) \right] + \frac{1}{6} B s_*^3 \theta (s_1^2 + s_1 s_2 + s_2^2) + B s_*^3 s_1 s_2 (s_1 + s_2) + \frac{1}{4} B s_*^3 (s_1^2 + s_1 s_2 + s_2^2)^2 - \frac{L}{a^2} s_*^2 \hat{s}_b^2 (\cosh^2 v - \cos^2 u) - \frac{1}{36} B s_*^3 s_b^3 \left( \frac{1}{3} - \sqrt{1-\theta} \right) \right\} \times \frac{a^2}{(\cosh^2 v + \cos^2 u)^2}, \tag{34}$$

where a prime $'$ denotes differentiation with respect to $v$, and both $s_1$ and $s_2$ have been scaled to $s_*$ while the same symbols are retained for them. In particular, the boundary conditions in Eq. (26) now read as

$$s_1|_{\partial\mathcal{B}} = -\tfrac{1}{3}\hat{s}_b, \quad s_2|_{\partial\mathcal{B}} = \tfrac{2}{3}\hat{s}_b, \quad \phi|_{\partial\mathcal{B}} = 0. \tag{35}$$

We introduce the biaxial coherence length $\xi_b$ as [13,16]

$$\xi_b := \sqrt{\frac{L}{Bs_b}} = \sqrt{\frac{L}{Bs_*(1 + \sqrt{1-\theta})}}. \tag{36}$$

It represents the length over which biaxial disturbances of the local order decay in space. This length clearly depends on temperature. The definition of $\xi_b$ is instrumental to give the free-energy functional $\mathcal{F}^*$ a more convenient, nondimensional form. If we further introduce the dimensionless variable

$$\eta := \frac{v}{v_c},$$

and we define

$$\hat{s}_1(\eta) := s_1(\eta v_c), \quad \hat{s}_2(\eta) := s_2(\eta v_c), \quad \hat{\phi}(\eta) := \phi(\eta v_c),$$

we can easily rewrite Eq. (34) as

$$\mathcal{F}^* = 2\pi B s_*^3 R^2 F[\hat{s}_1, \hat{s}_2, \hat{\phi}],$$

where

$$F[s_1, s_2, \phi] := \int_0^1 \left\{ \frac{\hat{s}_b}{v_c}\left(\frac{\xi_b}{R}\right)^2 [s'^2_1 + s'^2_2 + s'_1 s'_2 + (s_1 + 2s_2)^2 \phi'^2] + \hat{s}_b v_c \left(\frac{\xi_b}{R}\right)^2 \left[ (s_2 - s_1)^2 + \frac{3}{2} s_1 (s_1 + 2s_2)(1 - \cos 2\phi) - \hat{s}_b^2 \right] \times (2\coth(\eta v_c) - 1) + v_c \left(\frac{a}{R}\right)^2 \left[ \frac{1}{6}\theta(s_1^2 \right.$$

$$+ s_1 s_2 + s_2^2) + s_1 s_2 (s_1 + s_2) + \frac{1}{4}(s_1^2 + s_1 s_2 + s_2^2)^2 - \frac{1}{36}\hat{s}_b^3\left(\frac{1}{3} - \sqrt{1-\theta}\right)\Bigg]\frac{\cosh(\eta v_c)}{\sinh^3(\eta v_c)}\Bigg\} \mathrm{d}\eta, \tag{37}$$

and the hats $\hat{}$ have been dropped from all variables to avoid clutter. As a consequence of Eqs. (35), the functional $F$ is subject to the following conditions:

$$s_1(0) = s_1(1) = -\tfrac{1}{3}\hat{s}_b, \quad s_2(0) = s_2(1) = \tfrac{2}{3}\hat{s}_b, \qquad \phi(0) = \phi(1) = 0. \tag{38}$$

### B. Equilibrium textures

The final nondimensional form of the equilibrium equations, written in terms of the space variable $\eta$, are

$$2s_1'' + s_2'' = 2(2s_2 + s_1)\phi'^2 + v_c^2[2(s_1 - s_2) + 3(s_2 + s_1) \times (1 - \cos 2\phi)][2\coth(\eta v_c) - 1] + \frac{v_c^2}{6\hat{s}_b}\left(\frac{a}{\xi_b}\right)^2 \times (2s_1 + s_2)[\theta + 6s_2 + 3(s_1^2 + s_2^2 + s_1 s_2)] \times \frac{\coth(\eta v_c)}{\sinh^2(\eta v_c)}, \tag{39a}$$

$$2s_2'' + s_1'' = 4(2s_2 + s_1)\phi'^2 + v_c^2[2(s_2 - s_1) + 3s_1(1 - \cos 2\phi)] \times [2\coth(\eta v_c) - 1] + \frac{v_c^2}{6\hat{s}_b}\left(\frac{a}{\xi_b}\right)^2 (2s_2 + s_1) \times [\theta + 6s_1 + 3(s_1^2 + s_2^2 + s_1 s_2)]\frac{\coth(\eta v_c)}{\sinh^2(\eta v_c)}, \tag{39b}$$

$$\phi'' = -2\frac{\phi'(2s_2' + s_1')}{2s_2 + s_1} + \frac{3v_c^2 s_1}{2(2s_2 + s_1)}\sin 2\phi[2\coth(\eta v_c) - 1]. \tag{39c}$$

Equations (39) represent a sixth-order system of ordinary differential equations that we must solve subject to the homeotropic boundary conditions (38).

System (38) and (39) exhibits a singular point at the boundary $\eta = 0$, where $\sinh(\eta v_c)$ vanishes. Therefore, care must be taken to ensure that a well-behaved finite solution exists as $\eta \to 0$. It follows from the analysis of the order of divergence of the integrand in Eq. (37) that a solution to Eqs. (39) with finite energy must necessarily be such that both $s_1'$ and $s_2'$ vanish at $\eta = 0$. Furthermore, by a series expansion of (39) in the neighborhood of $\eta = 0$, we can show that bounded solutions exist provided $(s_1, s_2, \phi)$ take the following form, to second order in $\eta$:

$$s_1 = -\frac{1}{3}\hat{s}_b + 2\eta^2\left(\frac{v_c\xi_b}{a}\right)^2\left(\frac{4 - \theta + 4\sqrt{1-\theta}}{\sqrt{1-\theta}}\right) + o(\eta^2), \tag{40}$$

$$s_2 = \frac{2}{3}\hat{s}_b - 12\eta^2\left(\frac{v_c\xi_b}{a}\right)^2\left(\frac{1 + \sqrt{1-\theta}}{\sqrt{1-\theta}}\right) + o(\eta^2), \tag{41}$$

$$\phi = \phi'(0)\,\eta(1 - v_c\eta) + o(\eta^2). \tag{42}$$

In a neighborhood of $\eta = 0$, these analytical expansions are in extremely good agreement with the solutions obtained below.

The boundary value problem described by Eqs. (38) and (39) has been studied numerically for $1 < R/\xi_b < 10^3$. Smaller values of $R/\xi_b$ would be unphysical since $\xi_b$ is the smallest length scale in the problem and typically ranges between a few and ten nanometers [27]. Larger values of $R/\xi_b$, though perfectly acceptable, were more problematic for our numerical methods. Physically, our model explores the realm of cylinders in the nano-to-microscale range.

In all the following figures we have assumed that the reduced temperature is fixed, $\theta = -8$. This is a convenient exemplary case: all the qualitative features illustrated here persist for other values of $\theta$. We have obtained numerical solutions $(\hat{s}_1, \hat{s}_2, \phi)$ to the differential problem (38) and (39) for different values of biaxial coherence length $\xi_b$ and separation length $h$. In turn, this allows us to examine the eigenvalues of order tensor $\mathbf{Q}$ (subject to the appropriate rescaling).

In general, this problem exhibits two types of solution. For all values of the biaxial coherence length $\xi_b$, there exists a solution for $(\hat{s}_1, \hat{s}_2, \phi)$ such that $\phi(\eta) = 0$ for all $\eta \in [0,1]$. However, for separation lengths $h$ above some critical value, $h_c$, there exists a second type of solution with $\phi$ not identically zero. In this case, there is a rotation of the eigenframe of $\mathbf{Q}$ about $\boldsymbol{e}_u$. At the boundary of the region $\mathcal{B}$, that is, at the flat surface and cylinder, we have assumed uniaxial ordering with the director constrained to lie on the $(x,y)$ plane. Rotation of the eigenframe represents an *escape* of the equilibrium alignment into the $z$ direction in the bulk, analogous to the one occurring within two coaxial cylinders enforcing homeotropic boundary conditions on their lateral boundaries [28,29]. Actually, it follows from the symmetry of the equilibrium equations (39) under sign reversal of $\phi$ that there are indeed *two* escape textures differing by the sign of $\phi$: in the following, we shall select the positive $\phi$, bearing in mind that it also represents its symmetric companion. Both escape

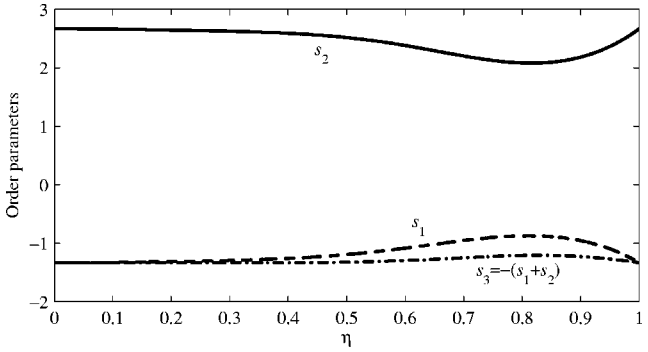


FIG. 2. The comparison of the eigenvalues of $\mathbf{Q}$ as defined in Eq. (24), rescaled to $s_*$ in Eq. (8) for the escape solution ($\phi \geqslant 0$). Here $h = 5R$ and $R = 2\xi_b$; the reduced temperature is $\theta = -8$.

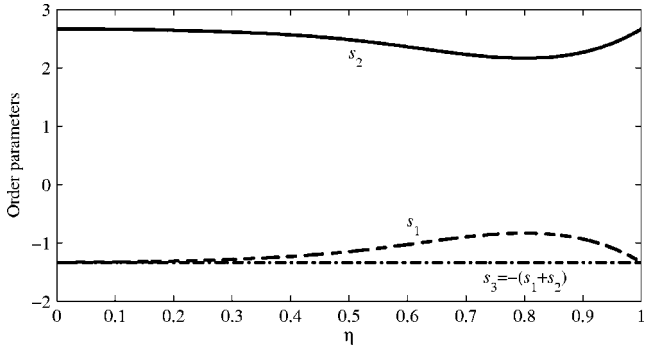


FIG. 3. The comparison of the eigenvalues of **Q** as defined in Eq. (24), rescaled to $s_*$ in Eq. (8) for the flat solution ($\phi \equiv 0$). Here $h=5R$ and $R=2\xi_b$; the reduced temperature is $\theta=-8$.

solutions are equally likely to arise when they minimize the renormalized energy $F$. As shown in the following section, in complete analogy with the analysis of the equilibrium tensor-order textures between coaxial cylinders [29], the escape solution is energetically favorable for $h \geqslant h_c$. To distinguish the escape texture from the other, we shall call the latter the *flat* texture.

The eigenvalues of **Q** associated with both types of solution are shown in Figs. 2 and 3. The corresponding angles $\phi$ are compared in Fig. 4. In both cases the order parameters deviate from their uniaxial equilibrium values close to $\eta=1$, i.e., in the neighborhood of the cylinder. This appears to be a curvature-induced effect due to the presence of fixed uniaxial ordering on the cylindrical surface.

By examining the degree of biaxiality $\beta^2$ defined in Eq. (3) for both the flat and escape profiles, as in Fig. 5, we can characterize the two cases. In general, there exists a curvature-induced element of biaxiality within the system, present regardless of the separation between cylinder and flat surface. However, if the separation is large enough, the director can escape into the third dimension in an attempt to retain its uniaxiality throughout the sample. The optimal rotation of the eigenframe is $\phi=90°$ as this would minimize $F$. The homeotropic surface constraints ensure that the actual maximum rotation achieved in the bulk is, generally, less than 90°. In Fig. 6 the maximum value $\phi_{\max}$ attained by the angle $\phi$ in the escape solution is plotted as a function of $h/R$: this graph indicates that $\phi_{\max}$ tends to 90° in the limit where the distance between the anchoring surfaces tends to infinity.

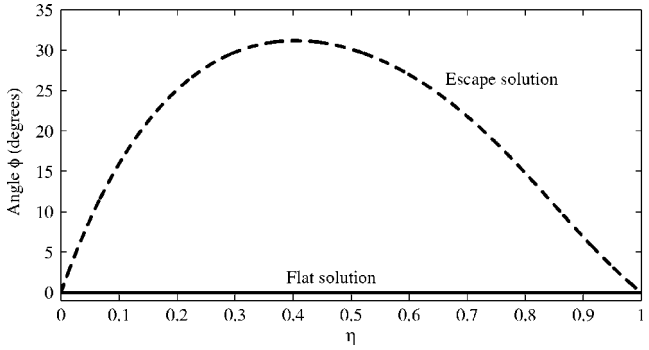


FIG. 4. The comparison of angle $\phi$ for escape and flat textures. Here $h=5R$ and $R=2\xi_b$; the reduced temperature is $\theta=-8$.

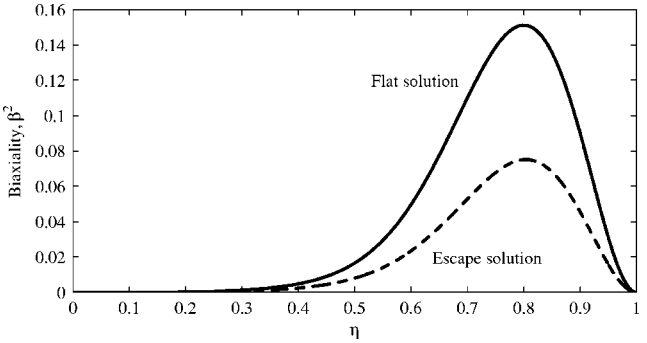


FIG. 5. The comparison of biaxiality $\beta^2$ as defined in Eq. (3) for escape and flat solutions. Here $h=5R$, $R=2\xi_b$, and $\theta=-8$.

As $R/\xi_b$ increases, the peak of biaxiality near the cylinder's lateral boundary (corresponding to $\eta=1$ in Fig. 5) becomes narrower and narrower, thus making the numerical solution of the equilibrium problem (38) and (39) more and more difficult. This is the reason why our analysis was not extended for $R/\xi_b > 10^3$.

## V. STABILITY

We have seen in Sec. IV that the equilibrium problem (38) and (39) possesses two solutions for $h \geqslant h_c$ and only one for $h < h_c$. Here we show that the critical value $h_c$ marks indeed a bifurcation. In Fig. 7, we plot the renormalized energy $F$ defined in Eq. (37) for both the flat and the escape solutions. For $h \geqslant h_c$, where both of these solutions exist, the escape texture is the global energy minimizer. Though the energy of the flat texture shown in Fig. 7 might appear to be almost independent of $h$, it is indeed a slowly increasing function of $h$, as illuminated by the close-up in Fig. 8.

The variation of the critical separation $h_c$ with the cylinder's radius $R$ is shown in Fig. 9. A bifurcation exists even at large $R$, albeit associated with a very small degree of biaxiality and eigenframe rotation. The critical separation is almost constant for large enough $R$, corresponding to a reduced biaxial influence. However, as the radius $R$ becomes comparable to $\xi_b$, the separation at which the escape rotation occurs appreciably increases.

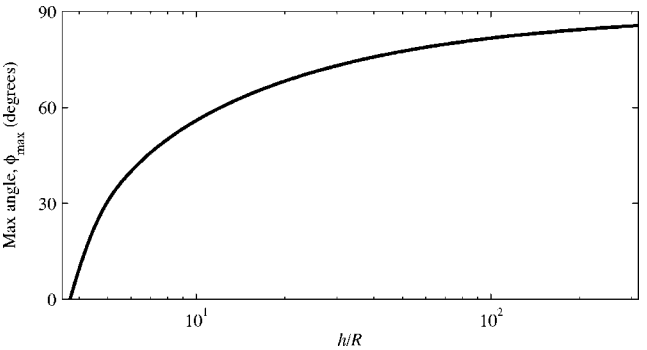


FIG. 6. The maximum value $\phi_{\max}$ of the angle $\phi$ for the escape solution as a function of $h/R$: $\phi_{\max}$ tends to 90 deg in the limit as $h/R \to \infty$. Here $R=2\xi_b$ and $\theta=-8$.

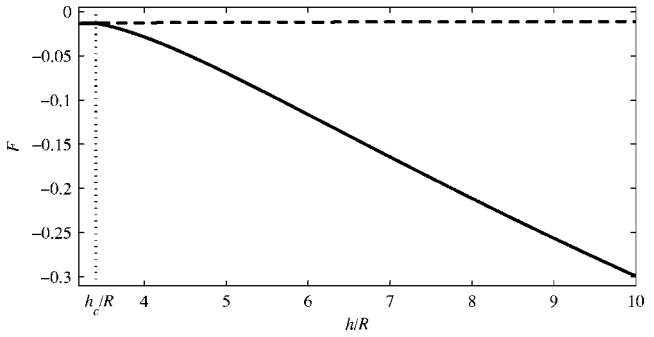


FIG. 7. The renormalized energy $F$ as defined in Eq. (37) for both the escape texture (solid line) and the flat texture (broken line) as functions of $h/R$. Here $R=2\xi_b$ and $\theta=-8$. For $h \geqslant h_c$, the escape texture is energetically favorable.

The asymptotic value of $h_c/R$ for large values of $R/\xi_b$ corresponds to a macroscopic limit that a purely director theory should also be able to capture through an analysis similar to that illustrated in Ref. [28]. We are not aware if such an analysis has been performed for the problem at hand here.

## VI. FORCE AND TORQUE

In this section we give the dimensional form of the formulas for both the force and the torque experienced by the cylinder. By computing the integral in Eq. (32) we see that the force $\boldsymbol{f}$ per unit height of the cylinder is given by

$$\boldsymbol{f} = \frac{2\pi L s_*^2}{R} f \boldsymbol{e}_y,$$

where

$$f := \frac{R}{a v_c^2}[s_1'(1)^2 + s_2'(1)^2 + s_1'(1)s_2'(1) + \hat{s}_b^2(\phi'(1)^2 + v_c^2)], \tag{43}$$

and $s_1$, $s_2$, and $\phi$ solve Eqs. (38) and (39). In a similar fashion, it follows from Eq. (33) that the moment $\boldsymbol{m}$ per unit height of the cylinder is given by

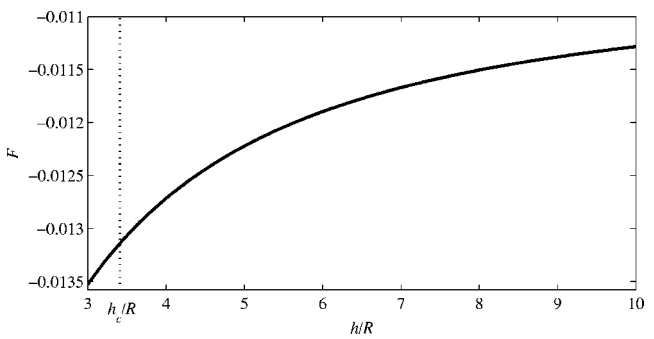


FIG. 8. A close-up of the graph of $F$ for the flat texture in Fig. 7. Clearly, this is a slowly increasing function of $h/R$.

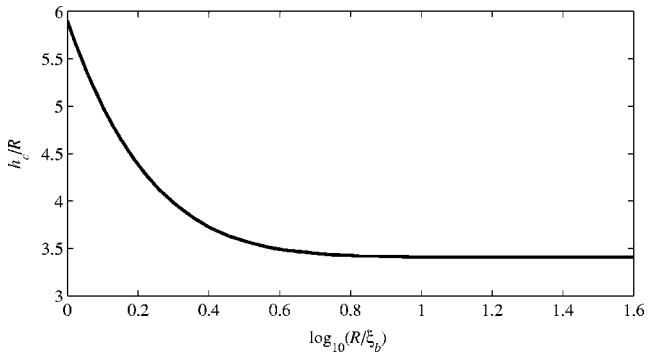


FIG. 9. The critical separation $h_c$ normalized to the cylinder's radius $R$ as a function of $R/\xi_b$. Here the reduced temperature is still $\theta=-8$.

$$\boldsymbol{m} = 4\pi L s_*^2 m \boldsymbol{e}_x, \quad \text{where} \quad m := \frac{\hat{s}_b^2}{v_c}(\cosh v_c - \sinh v_c)\phi'(1). \tag{44}$$

Both $f$ and $m$ have been evaluated for the two equilibrium solutions found above for different values of the separation $h$. Figure 10 examines the force and torque as the separation length varies. For the flat solution the derivative of $\phi$ is identically zero, therefore the torque is also identically zero. It is clear that the bifurcation associated with the exchange in energy is also characterized by distinct branches in the force and torque plots. The escape solution corresponds to a larger force on the cylinder and an increase in the magnitude of the torque.

Perhaps more significant, though, are the stationary points and lack of monotonicity exhibited by the force and torque on the escape solution branches. As the separation length is reduced, but before the energy bifurcation separation $h_c$ is reached, first the magnitude of the torque and then the force

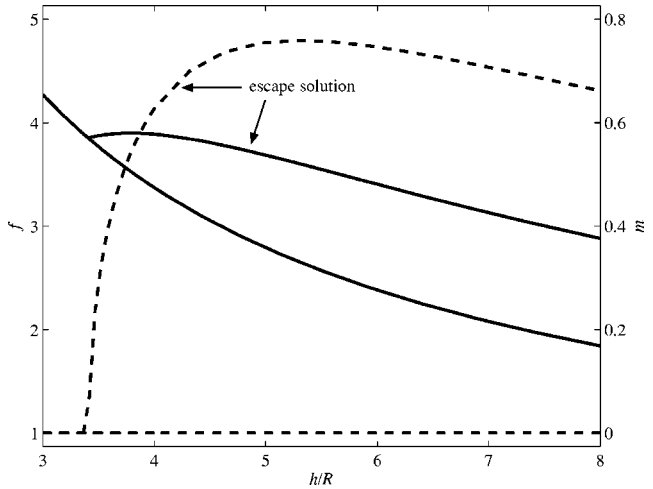


FIG. 10. The scaled magnitudes $f$ and $m$ of the force and torque experienced by the cylinder per unit height due to the presence of the liquid crystal. Here $R=10\xi_b$ and $\theta=-8$. For $h \geqslant h_c$, $f$ and $m$ are plotted against $h/R$ for both flat and escape solutions. The graphs of both $f$ (———) and $m$ (---) exhibit a significant lack of monotonicity.

experience maxima. This lack of monotonicity is very significant as it would impact upon any experimental apparatus which gradually reduces the separation length. For example, as the distance between plate and cylinder is reduced, the magnitude of the force required to maintain the separation gradually increases. However, there exists a *snapping* instability at a critical separation where the required force suddenly decreases; there is a similar instability and critical separation for the torque. The two critical snapping lengths are distinct, though the bifurcation distances $h_c$ are the same.

In particular, along the escape solution, the value of the distance $h$ at which the torque $m$ attains its maximum is larger than the one at which the force $f$ attains its maximum. This closely resembles the hierarchy exhibited by torque and force on the plates of a twist cell whose thickness is reduced down to values comparable to $\xi_b$ [27]. Like there, the instability that we predict here would be more easily detected by a *torque* machine rather than by a force machine. There would be another difference in the behavior of these two ideal machines. Along the force diagram a tiny hysteresis loop is associated with the snapping instability: upon decreasing the separation $h$, the transition from the escape to the flat branch happens at a value of this distance larger than $h_c$, while it happens at $h=h_c$ on the reverse process. By contrast, upon decreasing $h$ along the torque diagram, $m$ falls straight from its maximum to zero. In principle, with two parallel cylinders enforcing homeotropic anchoring, both the snapping instability and the associated hysteresis loop could be observed in the force diagram, but the same instability would be more dramatic in the torque diagram.

Finally, it is interesting to consider the behavior of the force that arises along the flat solution, especially at small separations. This solution resembles that described within the director theory restricted to in-plane configurations for the director [30]. By adopting a geometry similar to ours and employing a Frank-Oseen energy, Sonnet and Gruhn [30] showed that the elastic force on a cylinder per unit length due to a uniaxial nematic liquid crystalline film behaves like $1/\sqrt{h}$ for $h$ small. Assuming that the force $f$ and the separation $h$ are related via power law $f \propto h^{\lambda}$, we can calculate the exponent as

$$\lambda = \frac{h}{f}\frac{df}{dh}. \tag{45}$$

When $f$ is not a power of $h$, the exponent $\lambda$ in Eq. (45) can be seen as the locally approximating power law. Figure 11 illustrates the behavior of $\lambda$ for different choices of $R$. For $R$ so large as to weaken the influence of curvature on the concentration of biaxiality around the cylinder, our results also support strongly the analysis of Sonnet and Gruhn. However, it is clear that curvature has a strong effect on the power law for smaller values of $R$, with a plateauing in exponent $\lambda$ close to the bifurcation separation $h_c$.

In Fig. 11, the exponent $\lambda$ has also been computed along the flat solution for $h \geqslant h_c$, where the escape solution is instead the energy minimizer. The graphs in Fig. 11 show that $\lambda$ tends to $-1$ as $h \to \infty$, for all values of the ratio $R/\xi_b$. Such an asymptotic behavior is also realized along the escape solution, as shown in Fig. 12, and it is consistent with the result valid for the force experienced by a +1 disclination far from a flat surface with homeotropic boundary conditions (see p. 174 of Ref. [31]).

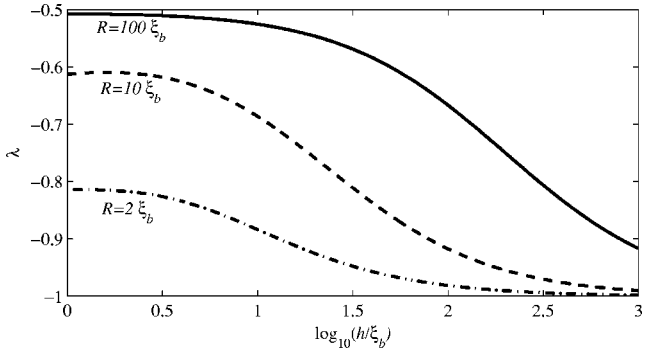


FIG. 11. Exponent $\lambda$ of the force as defined in Eq. (45) against separation $h$ along the flat solution. Here $\theta=-8$ and the ratio $R/\xi_b$ is chosen as 2, 10, and 100 in the three graphs. While $\lambda \to -\frac{1}{2}$ as $h \to 0$ only for $R/\xi_b=100$, $\lambda \to -1$ as $h \to \infty$ for all three values of $R/\xi_b$.

In our analysis so far cylinders have been treated as rigid. In the Appendix we also show the effect of the distributions of force and torque with uniform densities $\boldsymbol{f}$ and $\boldsymbol{m}$ on a linearly elastic, flexible cylinder.

## VII. CONCLUSIONS

We studied within the Landau–de Gennes theory the mechanical actions transmitted by a nematic liquid crystal on a submerged cylinder of radius $R$, under the assumption that the cylinder enforces homeotropic boundary conditions on the molecules of the surrounding liquid crystal. In particular, we studied the equilibrium problem that arises when the cylinder is kept at a prescribed distance $h$ from a plane wall also enforcing homeotropic boundary conditions. We heeded that the symmetry of this problem makes it equivalent to the one where two equal cylinders with parallel axes are surrounded by a nematic liquid crystal. We found that at a critical value $h_c$ for $h$ a bifurcation occurs among the equilibrium textures: for $h<h_c$, the minimum energy is attained on the equilibrium

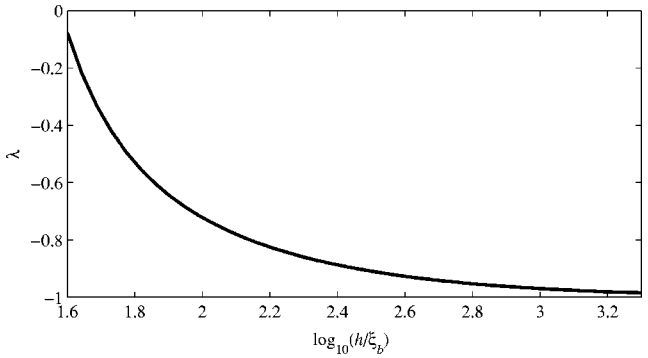


FIG. 12. The exponent $\lambda$ of the force as defined in Eq. (45) against separation $h$ along the escape solution. Here $\theta=-8$ and $R=10\xi_b$. As for all graphs in Fig. 11, $\lambda \to -1$ as $h \to \infty$.

solution where the order tensor **Q** has an eigenvector everywhere parallel to the cylinder's axis (flat solution), whereas for $h > h_c$ the minimum energy is attained on the equilibrium solution where the eigenframe of **Q** flips out of the plane orthogonal to the cylinder's axis (escape solution). The critical separation $h_c$ depends on the cylinder radius $R$ and saturates to a value slightly below $3.5R$ as $R$ grows larger than ten times the biaxial coherence length $\xi_b$. We computed the force and the torque transferred onto the cylinder at equilibrium, and we found that the diagrams of both against the separation $h$ are not monotonic and exhibit a maximum along the escape branch for $h > h_c$. This led us to predict a snapping instability with an associated hysteresis loop in the force diagram, which should occur upon steadily reducing $h$. The estimate for $h_c$ represents a lower bound for the value of $h$ at which the snapping instability is to be expected.

A similar instability was already predicted to occur in a twist cell when the cell's thickness approaches a critical value comparable with $\xi_b$ [27], although it appears to be different from the one predicted here. While the texture that eventually prevails in the twist cell for small separations between the plates bears the largest degree of biaxiality in the middle between the plates, the texture prevailing here for small separations between the cylinder and the wall bears the largest degree of biaxiality in a layer adjacent to the cylinder's lateral boundary. This supports our interpretation that here the texture bifurcation and the snapping instability that heralds it are driven by the cylinder's curvature, whereas the similar phenomenon in the twist cell is a clear signature of an order reconstruction taking place within the liquid crystal.

We are aware of a recent experiment [32] where a nematic liquid crystal is placed between two crossed cylinders: one cylinder enforces homeotropic boundary conditions, while the other enforces degenerate planar boundary conditions. This arrangement is somewhat intermediate between the model for the twist cell recalled above [27] and the model described here. Some evidence seems to emerge from the experiment that supports the existence of a snapping instability, though the small separations between the cylinders needed to experience it make the interpretation of the experimental data questionable. It would be desirable that an experimental study be undertaken with equal homeotropic anchorings on two parallel cylinders, since our model predicts in this case a snapping instability at larger separations.

## ACKNOWLEDGMENTS

We wish to thank R. Rosso and A.M. Sonnet for enlightening discussions. G. McKay wishes to thank the Carnegie Trust for Scotland and the Italian INdAM for financial assistance during his visit to the University of Pavia.

## APPENDIX: FLEXIBLE NANOCYLINDERS

Suppose that the nanocyliders studied in this paper can be modeled as linearly elastic, flexible rods, straight in their undeformed configurations. Let $\{x=0, y=h, 0 \leqslant z \leqslant \ell\}$ be the reference configuration of such a rod. Further assume that both ends at $z=0$ and $z=\ell$ are clamped, so that the tangent to all admissible configurations is there parallel to $\boldsymbol{e}_z$.

The equilibrium configurations of this rod are described by the equations

$$\boldsymbol{\Phi}' + \boldsymbol{f} = \mathbf{0}, \tag{A1}$$

$$\boldsymbol{\Gamma}' + \boldsymbol{t} \times \boldsymbol{\Phi} + \boldsymbol{m} = \mathbf{0}, \tag{A2}$$

where $\boldsymbol{f}$ and $\boldsymbol{m}$ are the linear densities of external forces and torques, $\boldsymbol{\Phi}$ and $\boldsymbol{\Gamma}$ are the linear densities of internal forces and torques, $\boldsymbol{t}$ is the tangent unit vector to the deformed configuration of the rod, and a prime here denotes differentiation with respect to arc-length in the deformed configuration. In Eqs. (A1) and (A2), $\boldsymbol{f}$ and $\boldsymbol{m}$ are to be expressed as in Eqs. (43) and (44). Two equal, unknown forces $\boldsymbol{F} = -F\boldsymbol{e}_y$ applied at the end-points of the rod balance $\boldsymbol{f}$ and $\boldsymbol{m}$.

Letting $\boldsymbol{\Gamma} = Bc\boldsymbol{e}_x$, where $B$ is the bending rigidity of the rod and $c$ is the local curvature of the deformed rod, under the usual assumption of small deformations, we arrive at the following solutions of Eqs. (A1) and (A2):

$$\boldsymbol{\Phi}(z) = \left( F - 2\pi L s_*^2 \frac{z}{R} \right) \boldsymbol{e}_y,$$

$$y(z) - h = \frac{\pi L s_*^2}{12B} \left[ -\frac{z^4}{R} - z^3 \left( 2 - \frac{\ell}{2R} \right) + z^2 \ell \left( 12 - \frac{\ell}{R} \right) \right],$$

where the function $y(z)$ represents the deformed rod. Thus, in particular,

$$F = \frac{\ell \pi L s_*^2}{R}$$

and

$$y(\ell) - y(0) = \frac{3\pi \ell^3 L s_*^2}{B}.$$

[1] H. Stark, Phys. Rep. **351**, 387 (2001).
[2] P. Poulin, H. Stark, T. C. Lubensky, and D. A. Weitz, Science **275**, 1770 (1997).
[3] P. Poulin, V. Cabuil, and D. A. Weitz, Phys. Rev. Lett. **79**, 4862 (1997).
[4] T. C. Lubensky, D. Pettey, N. Currier, and H. Stark, Phys. Rev. E **57**, 610 (1998).
[5] J.-C Loudet, P. Barois, and P. Poulin, Nature (London) **407**, 611 (2000).
[6] J.-C. Loudet and P. Poulin, Phys. Rev. Lett. **87**, 165503 (2001).
[7] A. Borštnik Bračič, K. Kočevar, I. Muševic, and S. Žumer, Phys. Rev. E **68**, 011708 (2003).
[8] C. Lapointe, A. Hulgren, D. M. Silevitch, E. J. Felton, H. D.

Reich, and R. L. Leheny, Science **303**, 652 (2004).
[9] J. L. Ericksen, Arch. Ration. Mech. Anal. **9**, 371 (1962).
[10] F. Brochard and P. G. de Gennes, J. Phys. (Paris) **31**, 691 (1970).
[11] F. Alouges and B. D. Coleman, J. Phys. A **32**, 1177 (1999).
[12] P. Kaiser, N. Wiese, and S. Hess, J. Non-Equilib. Thermodyn. **17**, 153 (1992).
[13] F. Bisi, E. C. Gartland, R. Rosso, and E. G. Virga, Phys. Rev. E **68**, 021707 (2003).
[14] A. Šarlah and S. Žumer, Phys. Rev. E **60**, 1821 (1999).
[15] S. Kralj and E. G. Virga, J. Phys. A **34**, 829 (2001).
[16] S. Kralj, E. G. Virga, and S. Žumer, Phys. Rev. E **60**, 1858 (1999).
[17] E. C. Gartland and E.. G. Virga, (unpublished).
[18] E. G. Virga, *Variational Theories for Liquid Crystals* (Chapman and Hall, London, 1994).
[19] E. C. Gartland, A. M. Sonnet, and E G. Virga, Continuum Mech. Thermodyn. **14**, 307 (2002).
[20] A. M. Sonnet and E. G. Virga, Phys. Rev. E **64**, 031705 (2001).
[21] A. M. Sonnet and E. G. Virga, in *Rational Continua, Classical and New* edited by M. Brocato and P. Podio-Guidugli (Springer, Milan, 2002), p. 169.
[22] A. M. Sonnet, P. L. Maffettone, and E. G. Virga, J. Non-Newtonian Fluid Mech. **119**, 51 (2004).
[23] F. M. Leslie, Arch. Ration. Mech. Anal. **28**, 265 (1968).
[24] C. S. Ogilvy, *Excursions in Geometry* (Dover, New York, 1990).
[25] J. N. Israelaschvili, *Intermolecular and Surface Forces* (Academic, London, 1992).
[26] R. G. Horn, J. N. Israelaschvili, and E. Perez, J. Phys. (France) **42**, 39 (1981).
[27] F. Bisi, E. G. Virga., and G. E. Durand, Phys. Rev. E **70**, 042701 (2004).
[28] F. Bethuel, H. Brezis, B. D. Coleman, and F. Hélein, Arch. Ration. Mech. Anal. **118**, 149 (1992).
[29] P. Biscari and E. G. Virga, Int. J. Non-Linear Mech. **32**, 337 (1997).
[30] A. M. Sonnet and T. Gruhn, J. Phys.: Condens. Matter **11**, 8005 (1999).
[31] P. G. de Gennes and J. Prost, *The Physics of Liquid Crystals* (Clarendon, Oxford, 1993).
[32] B. Zappone, Ph. Richetti, R. Barberi, R. Bartolino, and H. T. Nguyen (unpublished).